



**HAL**  
open science

# Deformation of aluminum in situ SEM and full field measurements by digital image correlation: evidence of concomitant crystal slip and grain boundary sliding

Alexandre Dimanov, A El Sabbagh, J Raphanel, M Bornert, L Thien-Nga, S Hallais, A Tanguy

## ► To cite this version:

Alexandre Dimanov, A El Sabbagh, J Raphanel, M Bornert, L Thien-Nga, et al.. Deformation of aluminum in situ SEM and full field measurements by digital image correlation: evidence of concomitant crystal slip and grain boundary sliding. 2023. hal-04028561

**HAL Id: hal-04028561**

**<https://hal.science/hal-04028561>**

Preprint submitted on 14 Mar 2023

**HAL** is a multi-disciplinary open access archive for the deposit and dissemination of scientific research documents, whether they are published or not. The documents may come from teaching and research institutions in France or abroad, or from public or private research centers.

L'archive ouverte pluridisciplinaire **HAL**, est destinée au dépôt et à la diffusion de documents scientifiques de niveau recherche, publiés ou non, émanant des établissements d'enseignement et de recherche français ou étrangers, des laboratoires publics ou privés.

**Deformation of aluminum *in situ* SEM and full field measurements by digital image correlation:  
evidence of concomitant crystal slip and grain boundary sliding**

A.Dimanov<sup>a,§</sup>, A. El Sabbagh<sup>a</sup>, J. Raphanel<sup>a</sup>, M. Bornert<sup>b</sup>, L. Thien-Nga<sup>a</sup>, S. Hallais<sup>a</sup>, A. Tanguy<sup>a</sup>

<sup>a</sup>*Laboratoire de Mécanique des Solides, CNRS UMR 7649, École Polytechnique, F- 91128, Palaiseau Cedex, France.*

<sup>b</sup>*Laboratoire Navier, CNRS UMR 8205, Ecole des Ponts Paristech, F-77420 Champs sur Marne, France*

§ To whom correspondence should be addressed. *E-mail:* alexandre.dimanov@polytechnique.edu

All figures should be printed in color but Figs. 5, 14, 15.

## Abstract

Mechanical testing *in situ* scanning electron microscopy (SEM) has become a standard technique for multiscale micromechanical investigation of polycrystalline materials. Direct observation of developing strain heterogeneities allows identification of the active mechanisms and quantification of their respective contributions to the overall strain. We developed a novel experimental setup for thermomechanical testing *in situ* SEM, especially suited to full strain field measurements. These are based on digital image correlation (DIC), from the sample scale to the scales of the aggregate and the single grain. We present results obtained during simple compression, at controlled displacement rates and at temperatures up to 400°C, of nearly pure polycrystalline aluminum exhibiting randomly oriented coarse grains (ca. 300  $\mu\text{m}$  in size). Electron microlithography was applied to produce specific surface marking patterns appropriate for the different scales of interest. Full surface strain fields were obtained by digital image correlation (DIC) analysis. The localization patterns evidenced dominant crystal slip plasticity, but also substantial simultaneous and continuous activity of grain boundary sliding (GBS), the contribution of which increased with temperature. We therefore advocate that experiments such as these here presented are necessary to go beyond a description in terms of deformation mechanism maps, which attribute deformation to a single mechanism.

**Key words:** **1-Methods of investigation:** electron microscopy, micromechanics, stress/strain measurements, **2-Material and constituting phases:** aluminium alloys, **4-Investigated phenomena:** grains and interfaces, plasticity and temperature, **Other:** Digital Image Correlation

## 1.Introduction

Understanding and modeling viscoplastic deformation of polycrystalline materials is essential for the control of shape forming processes and, more generally, for estimation of the durability of functional metallic structures submitted to extreme thermomechanical solicitations. Viscoplasticity of polycrystalline metals and alloys involves several microphysical mechanisms operating in volume, such as twinning and crystal slip, or at interfaces and grain boundaries, such as grain sliding and/or migration. At high temperatures, crystal slip is accompanied by recovery processes such as dislocation climb, polygonization and dynamic recrystallization, which are controlled by volume diffusion. For fine grain sizes (typically less than 10  $\mu\text{m}$ ), high homologous temperatures and low

strain rates, grain sliding controlled by diffusional mass transfer may become the dominant mechanism [1]. The different mechanisms may operate simultaneously and their respective contributions to the overall strain depend on the thermodynamic and loading conditions (e.g. temperature, stress and/or strain rate magnitudes, chemical environment), but also on the microstructure (grain size and morphology, texture, second phases). For a given material and conditions, one may determine the dominant mechanisms on the basis of the widely used concept of deformation mechanisms maps, introduced in the seventies [2], [3], [4]. However, the construction of such diagrams implicitly assumes that the considered mechanisms are independent, that is acting in parallel and contributing additively to the overall strain. This assumption is not straightforward, because simultaneously occurring mechanisms necessarily interact and some may possibly cooperate. As an example, in the case of dislocation creep ([5], [6]) strain mostly relates to crystal slip, but diffusion controlled dislocation climb controls the overall steady-state creep rate. Another case is that of grain boundary sliding: substantial activity of grain boundary sliding is observed for coarse grained polycrystals even at conditions supposed, according to deformation mechanism maps, to promote solely crystal slip ([7], [8]). In fact, crystal plasticity is inherently anisotropic and the different slip systems are non-equivalent in terms of critical resolved shear stresses. Grain boundaries may therefore act as efficient barriers to slip transfer from a grain to another, thus inducing local plastic incompatibilities ([9], [10], [11], [12]). Therefore, macro-homogeneous flow of polycrystals often involves not only crystal slip but also limited contribution of local accommodation mechanisms, such as grain boundary sliding [13], [14] and/or migration involving diffusional mass transfer or mobile disconnections [15]. Realistic modeling of polycrystalline viscoplasticity is therefore subordinated to detailed understanding of the interactions between these different mechanisms. Most of the time, however, the microstructural observations allowing to identify the possible active mechanisms through their specific microstructural signatures are realized *post mortem*. Consequently, the chronology of activation and the interactions between the different mechanisms remain unclear. It is necessary instead to identify and quantify these processes by *in situ* monitoring at the appropriate scales. Full mechanical field measurements based on DIC is among the most suited experimental technique for *in situ* SEM micromechanical characterization down to the grain scale [16]. For instance, the localization patterns allow to identify the active mechanisms, to characterize their interactions and to calculate their respective contributions ([13], [14], [17]).

Over the last decade, we developed different setups for *in situ* thermomechanical testing in a SEM, specifically devoted to full mechanical field measurements ([13], [14]). The device allows to perform simple compression/traction and bending tests at both room and high temperatures. The principle of full field measurements by DIC relies on the presence of local contrasts within the material. Each material point may be defined uniquely based on a specific signature in terms of the surrounding local gray scale levels. These signatures are used as kinematic markers in order to determine the displacement fields during the mechanical

transformation. The contrasts can be natural [17] or artificial [18]. For single phase polycrystalline materials observed in SEM there are not enough natural contrasts. We have therefore developed different techniques to provide surface kinematic markers, according to the microstructure and the testing conditions. The most recent technique consists in dewetting by annealing previously deposited thin metallic films in order to obtain randomly dispersed metallic spheroids onto the observed surface ([13], [14], [19]). Depending on metal, film thickness, temperature and atmosphere the size and the density of spheroids can be controlled, which makes it particularly suitable for very fine grained microstructures [19]. In the present work we studied nearly pure aluminum, containing only 0.1 wt% Mn [20]. The starting material was extracted from the central part of rolled aluminum plates. Heat treatment at 500°C resulted in an equilibrated and nearly non-textured microstructure, with coarse grain sizes of several hundreds of micrometers. Electron microlithography was used in order to produce regular golden micro-grids onto the sample surface [18].

For the mechanical testing, we used an original setup that we specifically developed for *in situ* SEM simple compression at temperatures of up to 600°C. The apparatus design allows for observation over the entire specimen surface. Contact-less thermal monitoring and control is ensured by *in situ* infrared pyrometry, which is detailed in the next sections. Parallelepiped samples 4x4x6 mm<sup>3</sup> were axially shortened stepwise up to 10 % at temperatures ranging between room conditions and 400°C. High quality SEM images with several magnifications were acquired at each deformation step and further analyzed by DIC (CorrelManuV software), in order to obtain kinematic surface fields and calculate full in plane strain fields ([13], [18], [21], [22]). The experimental details and analytical procedures are given in the following sections.

## **2. Experimental and analytical procedures**

### **2.1. In-situ SEM thermomechanical testing stage**

The experimental setup is based on a previously developed homemade traction - compression rig ([18], [17], [14], [13]), adapted to the original sample holder stage of a QUANTA 650 FEG-ESEM. The microscope is equipped for EBSD (electron back scatter diffraction), with a HKL Nordlys II S camera operated with Aztek 3.1 and Channel 5 data post-processing software. The rig frame is machined out of stainless steel and is U-shaped in order to provide maximum accessibility to the loading column and the sample (Fig. 1 and 2). Compression is driven by a conventional DC-motor Mattke 3557-K024C (nominal rotation speed and torque of 3000 rpm and 0.040 N.m, respectively). A gearbox reduces the rotation speed while increasing the torque. Rotation transforms into translation thanks to a screw nut system and the crosshead glides on linear ball bearing along two stainless steel shafts. The crosshead is instrumented with a linear displacement sensor (optical rule type from Solartron), which is fixed on the frame and measures the displacements for a homemade controller allowing to apply loading

rates as low as  $0.1 \mu\text{ms}^{-1}$ . The loading capacity is 5 kN. The applied force is measured by a load cell from Ametek, inserted within the assembly of the loading column (Fig. 2). The compression stroke ranges within 12 mm.

The main technical developments in the present work are concerned with the heating parts and temperature monitoring. Our previous heating setup was based on radiative heat transfer, thanks to a tubular furnace enclosing sample and pistons, but only a restricted sample area was accessible to observation through a circular window [13]. In contrast, the present system is designed to offer the entire sample surface free for observation. For that purpose, two tubular furnaces are fitted to the pistons and the sample is solely heated by conduction. The two assemblies of pistons and their tubular resistors are thermally insulated by cylindrical ceramic shields (machined from pyrophyllite). We used SiC pistons which are connected to the rig frame with metallic wires, hence avoiding electrical charging of samples. Precise temperature monitoring is usually obtained by attaching or directly welding a thermocouple on the sample. In order to avoid any risk of local alloying, or loss of contact during sample deformation, we did not apply such technique. Temperature monitoring and control is ensured by contactless measurements realized with an infrared pyrometer installed within the SEM chamber and targeting the sample from aside (Fig. 1). The details are provided in the following section. The tests last several hours, so that a cooling circuit (mix of water and alcohol) is established to protect the electronics, load cell and actuator. The cooling circuit is composed of flexible silicone tubes connecting two stainless steel parts and a chiller centrifugal pump providing continuous cooling flow, the temperature of which is adjusted according to the experimental set point. For example, when the sample is heated at  $300 \text{ }^\circ\text{C}$  we regulate the water temperature at  $10 \text{ }^\circ\text{C}$ . One of the water cooled steel elements is inserted in-between the insulated heating element and the load-cell, which is attached to the frame. The other one is placed in-between the second insulated heating element and the cross-head of the loading column. All these elements are precisely aligned in order to avoid stress concentrations at the ceramic parts. The temperature of the load-cell is monitored by an RTD Pt100 sensor.

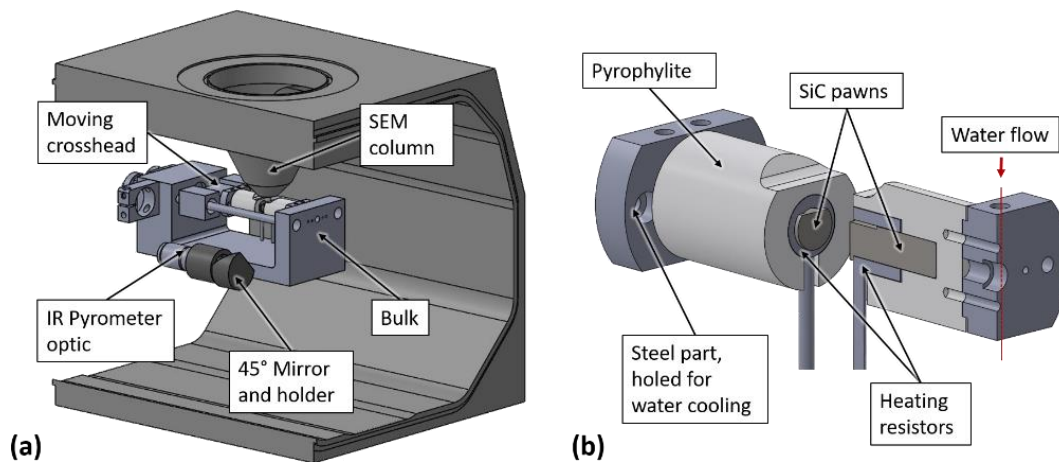


Figure 1: (a) Schematic view of the SEM chamber with the in-situ testing set up, composed of the deformation machine and the IR-pyrometer. (b) Magnification of the deformation column assembly, showing the two steel cross-heads with two SiC pistons surrounded by two heating coils (Pt resistor wires) and annealed pyrophyllite thermal shielding. The cross heads comprise a liquid cooling circuit.

A technical drawing of the heating elements is shown on Fig. 1(b). The heat is generated by two heating resistors with double sense wiring of  $1.1 \Omega$  each (40 W). The double sense wiring precludes development of magnetic fields which could disturb the electron beam. The resistors consist of platinum wires (0.3 mm in diameter) embedded in multi-layered ceramic insulation. The resulting tubular heating elements are 14 mm in length, with 7 and 13 mm inner and outer diameters, respectively. PID controlled current is provided by a switch-mode DC power supply (maximum output: 20V/20A). The heating elements are placed surrounding two sintered SiC pistons, chosen for their appropriate mechanical strength and thermal conductivity. Symmetrical heating of the sample is obtained by conduction through the pistons (Figures 1b and 2b), which have precisely flat and mirror polished end surfaces to ensure good contact and heat transfer to the sample, but also to reduce interfacial frictions. Insulating shields made of annealed pyrophyllite (aluminosilicate ceramic) limit radiative loss. The starting pyrophyllite material is soft and easy to machine in its naturally hydrated form. After machining the shield pieces are dehydrated by annealing at  $1300 \text{ }^\circ\text{C}$  for about 4 hours, reaching a compressive strength of the order of 800 MPa. The complete experimental setup is shown in Figures 1 and 2. The details on the *in situ* SEM pyrometer are given in the following section.

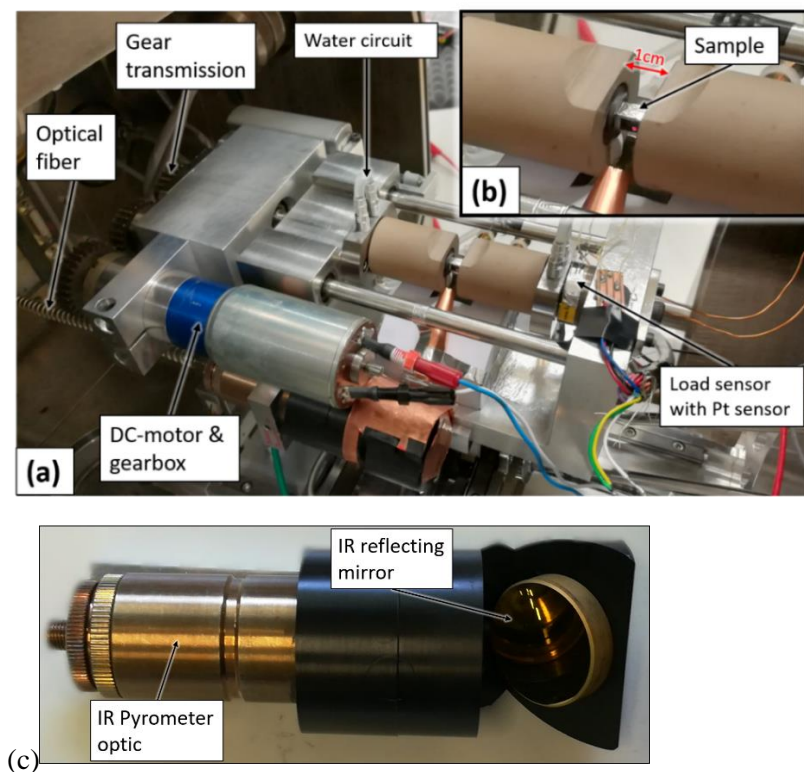


Figure 2: (a) Overall view of the SEM chamber with the in-situ testing machine mounted on the SEM platen. The pyrometer lies aside, under the motor. The steel elements of the fixed and mobile crosshead comprise cooling fluid circuits (b) Zoom on the central part of the loading column, composed of pyrophyllite insulators, shielding the Pt resistor coils, which surround the SiC pistons. (c): Optics and Lumasens IGA 320/23-LO pyrometer. The IR reflecting mirror is mounted on the black MACOR tilted holder. The whole assembly mounts on the mechanical testing stage, under the motor, as shown in (a). In order to avoid parasite IR radiations, the holder of the reflecting mirror is partially covered with copper foil. The mirror collects exclusively the radiations emitted by the targeted sample side, which is painted in black. In (b) one can see the red spot on the sample side where the pyrometer is focused.

## 2.2. Contactless temperature measurement and monitoring

The measurement of sample temperature without contact is a key development of our setup. On the one hand, the geometrical constraints of the heating concept preclude introducing a thermocouple close enough to the sample and leaving accessible the whole observation area. On the other hand, the aluminum sample and the experimental temperature range do not allow for easy welding or sticking of a thermocouple on the sample back side without risk of losing contact during loading. Therefore, we adapted an infrared pyrometer Lumasens IGA 320/23-LO for *in situ* SEM contactless measurements of sample temperature. The emitted infrared radiation is transmitted by a mirror to the optics of the pyrometer located in the SEM chamber, which is connected via an optical fiber to the detector and electronics located outside the SEM (Fig. 2). The optics' focal distance can vary from 8.8 cm to 11 cm, which allows an accurate focus on the sample's surface with a spot size of 0.8 mm. The considered wave lengths range between 2 and 2.6  $\mu\text{m}$ . Temperature measurement ranges between 100°C and 700°C, with an overall estimated precision within 3 °C. A mirror deflects the infrared radiations from the sample to the pyrometer optics, which are clamped aside the rig (Fig. 2). The pyrometer optics and the deflecting mirror are shown on Fig. 2c. The optical axis is aligned at 60° to the normal of the sample's side. The deflecting mirror is protected by a copper shield, in order to avoid parasite emissions from the chamber, the setup and more specifically from the heating elements. The only measured infrared signal is collected by a copper funnel operating as a waveguide from the sample side to the deflecting mirror (Fig. 2).

According to the Stefan-Boltzmann law the irradiance is proportional to the fourth power of the temperature. Therefore, the reading of the pyrometer corresponds to the intensity of infrared radiations within the considered wavelength range emitted by the sample. The emissivity coefficient  $\epsilon$  of the sample represents the ratio of its real radiative emission and that of the theoretical black body. Together with the Stefan-Boltzmann constant it represents the proportionality between radiation intensity and temperature. The higher is  $\epsilon$  and the better is the measurement. Metals are called selective bodies, because their emissivity coefficients are usually low, but also temperature and wavelength dependent. In the present case  $\epsilon$  may be assumed constant over the limited wavelength range. But for aluminum  $\epsilon = 0,3$ , which is very low. We improved the emissivity coefficient up to  $\epsilon = 0,64$  by spraying thermo-resistant black paint onto the sample surface targeted by the pyrometer optical line.

The pyrometer is initially calibrated for atmospheric conditions, that is at  $10^5$  Pa total air pressure, that is in the presence of water vapor, which is very absorbing in the wavelength range of interest. Therefore, we specifically calibrated the measurements for the high vacuum of the SEM chamber ( $10^{-3}$  Pa). We actually established corrections to the emissivity coefficient for each experimental temperature. For that purpose, we prepared a replica aluminum sample, of dimensions identical to these of the samples used for mechanical testing. K-type thermocouple was inserted within a borehole of 0.5 mm, that was drilled in the center of the sample. The corresponding temperature was used as reference for the pyrometer readout, while adjusting the emissivity coefficient parameter.

### 2.3. Material and sample preparation

According to previous works ([20], [23], [24]), the starting material is nearly pure aluminum, with only 0.1 wt. % of manganese. This alloying element reduces the mobility of grain boundaries by solute drag effect ([23], [24]). Thermal stability of the microstructure is important for *in situ* strain measurements, because migrating grain boundaries may i) obscure the contribution of pure grain boundary sliding, ii) limit the cumulative strain analysis. The slightly alloyed material is a single phase polycrystal with a face centered cubic structure. These characteristics allow for a precise analysis of the micro-mechanisms that take place in the course of plastic deformation ([9], [10]). The material has low melting point ( $667^\circ\text{C}$ ) and yield stress (a few MPa), and hence the setup permits exploration of a wide range of experimental conditions and activation of different potential mechanisms ([8], [9], [10], [11], [12], [24], [25]).

The starting material was furnished by Alcan CRV (ingot series 3442 C). Al-0.1Mn slabs of  $100\times 60\times 20$  mm were cold rolled up to 0.5 total strain. The lamination process was realized at the Laboratoire Georges Friedel (Ecole des Mines de Saint Etienne, [24]). The samples are cut out from the central part of cold rolled slabs in order to limit microstructural gradients due to boundary effects. Samples are parallelepiped shaped ( $4\times 4\times 6$  mm<sup>3</sup>), with the rolling direction parallel to their longest dimension, which is also meant to be the compression axis. Annealing at  $500^\circ\text{C}$  for 20 - 30 minutes strongly reduces the initial rolling texture, and results in a fairly homogeneous and equiaxed recrystallized microstructure. In spite of the Mn solute, at such high temperature mobility of grain boundaries is fast enough, so that we obtain a coarse grained and equiaxed microstructure. The mean grain size obtained by the intercept method is of  $300\ \mu\text{m}$  and shows a mean aspect ratio of 1.2. The grain size distribution is unimodal, but spread (100 -  $1000\ \mu\text{m}$ , Fig. 3).

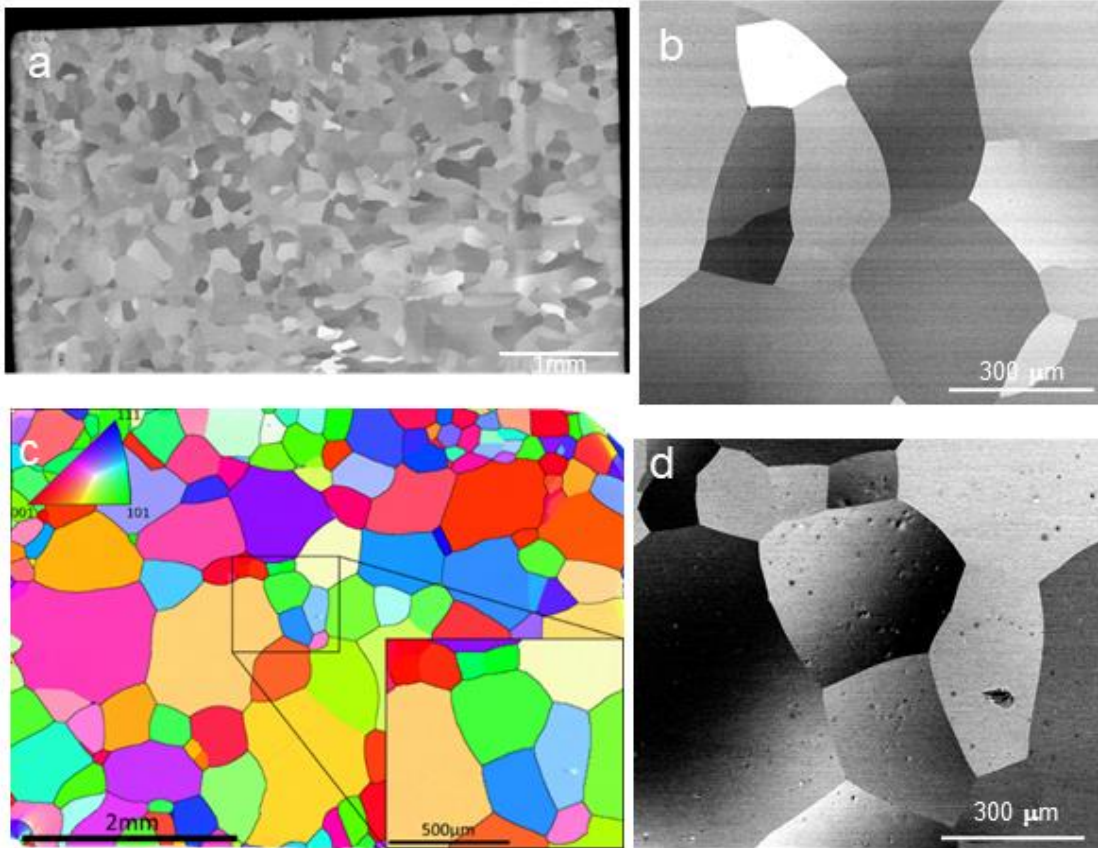


Figure 3: Sample microstructure. a: Large view of a typical aluminum sample (4x4x6 mm<sup>3</sup>), reconstructed from SEM micrographs in Z-contrast mode. b: Closer view of the microstructure (SEM Z-contrast mode). c: Inverse pole figure (IPF) map with respect to the compression axis (horizontal) from an EBSD scan of a sample surface (4x6 mm<sup>2</sup>). The IPF color reference is inserted in the upper left corner. The central area of 1 mm<sup>2</sup>, enlarged at the lower right corner, is the main region of interest (ROI-1) which is studied in details by DIC and which SEM micrograph in Z-contrast mode is shown in (d). One can see some etch pits resulting from the electrolytic treatment which may sometimes perturb the EBSD indexations (see the North-South elongated light blue grain).

The annealed samples are first mechanically polished with SiC grinding papers down to 4000 grade (5 μm particle) and secondly with diamond paste down to 3 μm. Mirror quality finish is obtained by electro-polishing with a commercial STRUERS A2 electrolyte solution. The procedure removes the cold worked zone, ensuring a good crystalline surface state adequate for EBSD (electron backscatter diffraction) analysis (Fig. 3a), but may result in some etch pits as shown in Figure 3d. For each sample we choose a representative region of interest (ROI), of 1 mm<sup>2</sup> with homogeneous and non-textured microstructure, such in Figure 3b.

## 2.4. Digital image correlation

DIC (digital image correlation) is a computational technique, aiming at the characterization of the mechanical transformation relating an image from an actual (deformed) state to an image from a previous (reference) state. In our case we applied 2D DIC, which implies solely the characterization of in plane strain.

The DIC method relies on the existence of contrasts, that is variable local grey scale levels, which can be assigned to the surficial material points as characteristic signatures. In practice the procedure aims to determine the surficial displacement field of material points that are discretely distributed following a periodic pattern like a grid. These measurement points are centered within restricted domains, called correlation windows, which grey scale level is considered as the discriminative signature of the measurement point. The in plane displacement field corresponding to the mechanical transformation between the reference and the actual states is obtained by the minimization of the so called correlation coefficient, defined on the basis of the grey scale levels of the reference and actual states. The corresponding in plane transformation gradient is computed following different local integration schemes, based on a contour integral defined by a chosen number (usually from 2 to 8) of nearest neighboring measurement points. The computation of the in plane strain components depends on some strong hypotheses, namely volume conservation, or axisymmetric deformation. The accuracy of strain computation increases with the number of considered neighboring points (large contour integral). Conversely, the resolution of the computed strain field decreases due to the increasing local gage length (for details see [13]).

In our case, the local contrasts are provided artificially. We applied SEM micro-lithography for the deposition of thin ductile metallic grid patterns onto the observed surfaces of the samples. We will not elaborate on the details of the technique, which is well documented in the literature ([18]). But, we must specify that the choice of the metal to be deposited depends on its stability with respect to the substrate and the experimental temperatures. The grid marking patterns are usually made of gold. However, gold alloys with aluminum and thin gold films are easily dewetting at temperatures of 400°C and above ([13]). Therefore, instead of gold our choice came to platinum.

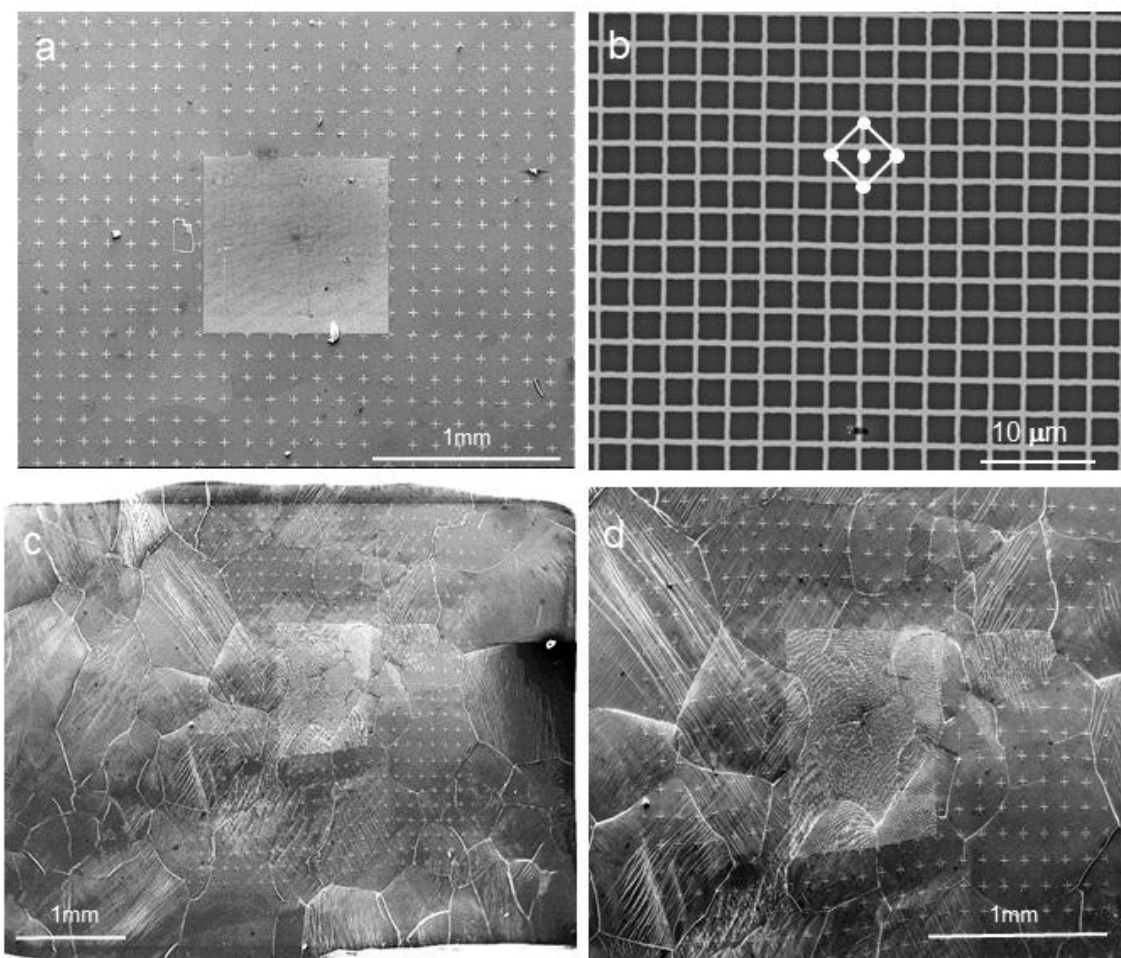


Figure 4: SEM micrographs showing the two-scale typical patterns of platinum deposit obtained by electron-microlithography (before and after deformation). a: Crosses are distant by  $125\ \mu\text{m}$  one from another (gage length  $250\ \mu\text{m}$ ) and cover the ROI-2 of  $3\times 3\ \text{mm}^2$ . ROI-1 covers  $1\times 1\ \text{mm}^2$  in the middle of ROI-2. b: Detail of the central grid pattern of ROI-1, with  $3\ \text{mm}$  pitch. The pattern is used to calculate the local strain fields at the measurement points corresponding to the grid intersections. The strain computation contour is based on the nearest 4 neighbors, as schematically indicated in the middle of the image, hence resulting in a local gage length of  $6\ \mu\text{m}$ . c: Low magnification view of a whole specimen deformed at  $300^\circ\text{C}$  up to 5% horizontal shortening. d: Central part of the specimen in (c). The crosses-marked ROI-2 allows to compute the strain field with low resolution, (but high accuracy) over a large area and to quantify the average sample shortening. The central grid-marked ROI-1 allows to compute highly resolved full strain fields, in order to identify and quantify the deformation mechanisms.

In practice, the measurement points of the computational array can be centered at the intersections of the surficial platinum grid, as shown schematically in Figure 4b. In this present case, the chosen configuration of 4 neighbors defines a lozenge-shaped integration contour. The resulting local gage length of  $6\ \mu\text{m}$  determines the spatial resolution of the in plane computed strain field. The Pt surficial grid pitch may be adjusted depending on

the resolution wanted for the computed in plane strain field. We have selected two regions of interest. ROI-1 represents  $1 \text{ mm}^2$  centered within the sample observation surface ( $6 \times 4 \text{ mm}^2$ ). ROI-2 represents  $3 \times 3 \text{ mm}^2$  surrounding ROI-1. ROI-2 excludes the sample borders that may be concerned with end effects and fretting, but remains large enough to be representative of the strain experienced by the specimen as a whole. The mean strain components are computed over the ROI-2 with a large gage length (ca  $250 \text{ }\mu\text{m}$ ), masking fine scale heterogeneities, but ensuring computational accuracy and rapidity. Nearly real-time DIC can be performed at the mesoscopic scale over ROI-2, providing a better monitoring of the deformation process than relying on the displacement sensor of the cross-head, which measurement is affected by the compliance of the mini-rig. The pattern of the deposited platinum covering the ROI-2 represents a regular grid of crosses with a pitch of  $125 \text{ }\mu\text{m}$  (Fig. 4), that remains substantially lower than the mean grain size (ca  $300 \text{ }\mu\text{m}$ ). ROI-1 is selected with respect to the homogeneity of the microstructure and the absence of remaining texture. The pattern of the deposited platinum covering the ROI-1 represents a continuous regular grid. This domain is meant for detailed investigation of strain heterogeneities and active mechanisms at the scales of the individual grain and the aggregate. The grid pitch is therefore reduced down to  $3 \text{ }\mu\text{m}$  (Fig. 4), allowing computing with fine gage lengths (ca  $6 \text{ }\mu\text{m}$ ) and providing highly resolved strain fields. The grid lines are  $600 \text{ nm}$  wide, which represents a few pixels in length for the micrographs with resolution of  $4096 \times 3775$  pixels.

The fine scale grid of ROI-1 shown in Figure 4 exhibits a Moiré effect, due to the combination of subsampling (e-beam spot size smaller than pixel size) and slight misalignment between the marking grid and the scanning direction. The Moiré effect can be attenuated with application of a Gaussian filter during post-processing.

The grid of measurement points devoted to DIC is adapted to the different marking patterns for ROI-1 and ROI-2. For the former and latter ones the measurement points are located onto the intersections of the grid and onto the crosses, that is spaced by 12 and 171 pixels, respectively. For ROI-1, the correlation windows are  $12 \times 12$  pixels, and hence the whole area is covered without overlapping of neighboring windows, which prevents smoothing of strain heterogeneities. The subpixel correlation is performed with a bilinear interpolation ([21], [22]).

## 2.5. Strain computation

The DIC procedure delivers the displacement field of the measurement points, which allows strain computation. The integration contour we used to compute the local strain at each point is diamond shaped. It is defined by the 4 nearest neighboring points (integration scheme 2, as defined in [13]). The grid of points has a pitch of  $3 \text{ }\mu\text{m}$ , therefore the local gauge length is of  $6 \text{ }\mu\text{m}$  (see Fig. 4b).

The DIC provides only the in plane displacements and thus we can only compute the corresponding components of the in-plane transformation gradient  $\mathbf{F}$ :  $F_{11}$ ,  $F_{22}$ ,  $F_{12}$ ,  $F_{21}$ . In order to compute the strain tensor some

assumptions are necessary in the framework of small strains. First, the normal to the observation plane is considered to be a principle axis of deformation and no out-of-plane rotations are considered, which implies  $F_{13} = F_{31} = 0$ . The last hypothesis assumes axisymmetric conditions (transverse isotropy), which allows to compute the out-of-plane strain component.

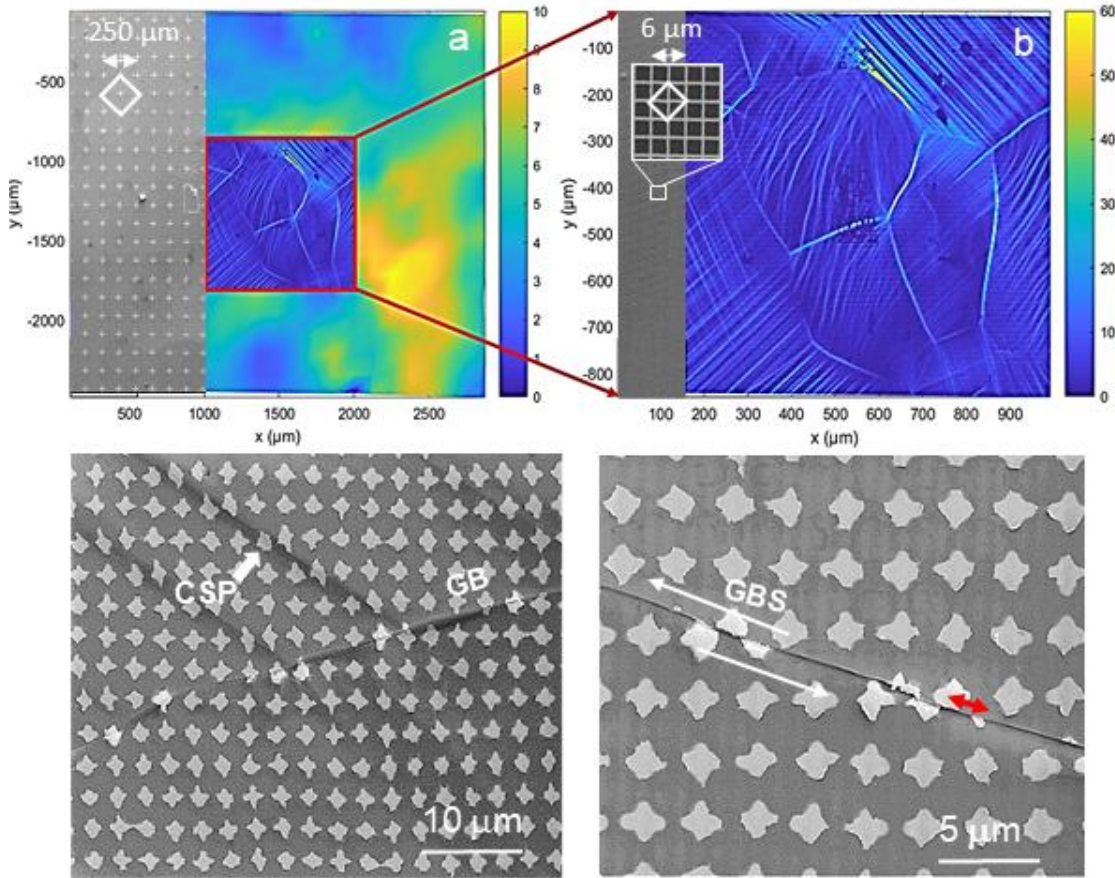


Figure 5: Computed strain maps corresponding to the ROI-2 and ROI-1 shown in Figure 4a, representing the “von Mises” equivalent strain map (in percent), for an in-situ test at 200°C at 5% overall axial shortening. a: The strain field of the 3 mm large ROI-2 is poorly resolved, owing to the rough surface marking: the array of Pt crosses shown on the left hand of the map implies a large gage length of 250 μm (see text). It allows for a fast and accurate computation of the overall strain. b: The 1 mm large ROI-1 (centered within ROI-2) has a fine scale marking (Pt grid, shown on the left hand of the image), allowing for a gage length of 6 μm, and hence a highly resolved strain field showing strain localization at the grain scale. Localizations happen in a discrete manner within individual grains, due to activation of crystal slip plasticity (CSP). Crystal slip bands are shown in higher magnification in (c). Grain boundary sliding (GBS) is also evidenced by localization at some interfaces (see text). GBS is shown in (d). The red double arrow shows the offset resulting from GBS. Note that in (c) and (d) the markers are small size irregular crosses: an alternative to the regular grid.

Two examples of strain computation at the scales of ROI-1 and ROI-2 are shown in Figure 5. Their respective local strain gages are of 6  $\mu\text{m}$  and 250  $\mu\text{m}$ , and hence the corresponding resolutions. The concerned test was performed at 200°C, until axial shortening of 5 %. The mean axial strain component is computed in real time during the test over the whole ROI-2 domain. The strain maps presented in this work show a scalar representation of the local plastic deformation. We use the second invariant of the deviatoric part of the in-plane strain tensor, which is the 2D analog to the von Mises equivalent strain. With the above mentioned assumptions it may be written as  $\varepsilon_{\text{eq}} = 2|\varepsilon_1 - \varepsilon_2|/3$ , where  $\varepsilon_1$  and  $\varepsilon_2$  are the in-plane principal strain components.

## 2.6. Testing protocol

A strict testing protocol was developed to ensure the reproducibility of the results. At first, the cooling circuit is stabilized at the cooling temperature corresponding to the testing high temperature, as established during the calibration procedures. Secondly, the load cell is preloaded at 100 N, the sample is inserted in between the SiC pistons, where it is maintained with an additional preload of 10 N.

Correct sample positioning requires the observation surface and the painted lateral facet to be perpendicular to the SEM column and to the pyrometer optical line, respectively. The pyrometer alignment is tuned by focusing its in-built LED onto the painted sample face. When vacuum reaches  $10^{-3}$  Pa, the sample emissivity parameter is set to the value corresponding to the desired temperature (according to our calibration, see section 2.2) and the heaters are powered. During the heating and thermal expansion phase, the crosshead position is adjusted to maintain the pre-loading of the sample around 10 N. Equilibrium temperature is reached within less than an hour. The electron beam is set at 15 kV.

The initial state micrographs are the references for the correlation procedures. The reference state is also used to estimate the systematic errors, through the analysis of a known transformation, introduced by small variations of magnification.

The deformation is realized stepwise, by increments of about 0.5 % axial strain, at controlled crosshead displacement rate of 0.1  $\mu\text{m s}^{-1}$  corresponding to a strain rate of about  $10^{-5}$   $\text{s}^{-1}$ . The axial crosshead displacement is controlled by the displacement sensor, whilst the total average axial strain is monitored by a quick DIC computation, performed over the 3 mm - wide area (ROI-2) marked by crosses (Fig. 4 and 5). Higher magnification micrographs are further collected over the central 1 mm – wide ROI-1 area, marked by fine grids or dots, in order to compute later on highly resolved full strain fields (Fig. 4 and 5).

### 3. Results and discussion

The DIC-based full strain field computations which are realized over the larger 3 mm - wide areas (ROI-2) enable to extract precisely the total average axial strain for the central part of the specimen. The computed data and the macroscopic stress (considering applied force and actual sample cross section) are used to plot the characteristic loading curves of strength versus axial strain shown in Figure 6. The advantages of such measurements with respect to the usual macroscopic records of strain by displacement sensors are to exclude machine-related effects (emplacement of the loading column and frame compliance), but also to limit the sample-scale strain heterogeneities related to piston fretting effects. The loading curves correspond to room temperature and three high temperatures: 110, 200 and 300°C, representing respectively homologous temperatures of 0.4, 0.5 and 0.6. Yield stresses and strain hardening rates decrease with increasing temperature. This behavior is typical for thermally activated dislocation recovery processes, among which dynamic recrystallization, which is highly dependent on strain rate and temperature ([25], [26]), The aspects will be addressed in more details in the next sections on the basis of the obtained strain maps.

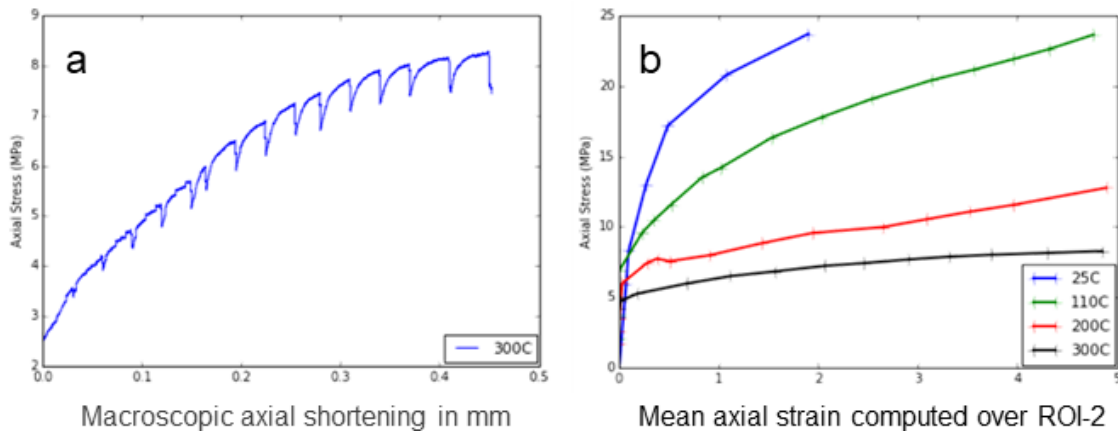


Figure 6: Mechanical curves for AlMn0.1 compressed at different temperatures. a: Raw loading curve based on the data recorded by the load cell and the linear displacement sensor attached to the mobile crosshead. b: Stress - Strain curves for 25°C, 110°C, 200°C and 300°C based on the data recorded by the load cell and the mean strain computed over the large central ROI-2 zone (see Figures 3, 4 and 5). The raw step-by-step loading curve represents the mechanical behavior of the sample combined with the compliance of the machine and the emplacement of the loading column. Conversely, the computed Stress-Strain curves represent solely the mean effective strain of the large central area of the sample (ROI-2). Note the relaxation of the material during the time lapse corresponding to imaging after each loading steps.

#### 3.1. Influence of temperature

Figure 7 summarizes the results of uniaxial compression tests performed at ambient 25°C, 110°C, 200°C and 300°C, that is respectively  $0.3T_m$ ,  $0.4T_m$ ,  $0.5T_m$  and  $0.6T_m$ . Figures 7a to 7d present the equivalent von Mises strain maps computed by DIC over the central 1 mm-wide area (ROI-1) for the final deformation step,

cumulating axial strains of c.a. 2 % for room temperature and c.a. 5 % for higher temperatures. Note that the color scale, given in strain %, is not the same for all the tests.

Figures 7e and 7f show the Z-contrast and secondary electrons micrographs corresponding respectively to the original microstructure and the deformed state (with marker grid) of the specimen deformed at 110°C. Both the SE micrographs and the DIC-computed equivalent strain maps allow to see the activation of crystal slip in the individual grains. The SE micrographs exhibit surface slip lines characterized by step-like topography, that we call “physical slip lines” (PSL), resulting from out of plane slip components. Conversely, the DIC-computed strain maps evidence the in-plane slip components of active slip systems. When both components are present, both observations reveal the same slip lines. But, in extreme cases, when the out-of-plane component of a slip system is negligible, the slip lines are evidenced solely by the DIC-computing procedure. We will call the corresponding slip lines “kinematic slip lines” (KSL), as they do not leave any remaining physical signature. The traces of KSL and PSL are therefore complementary for identifying all the active slip systems, which will be discussed later on.

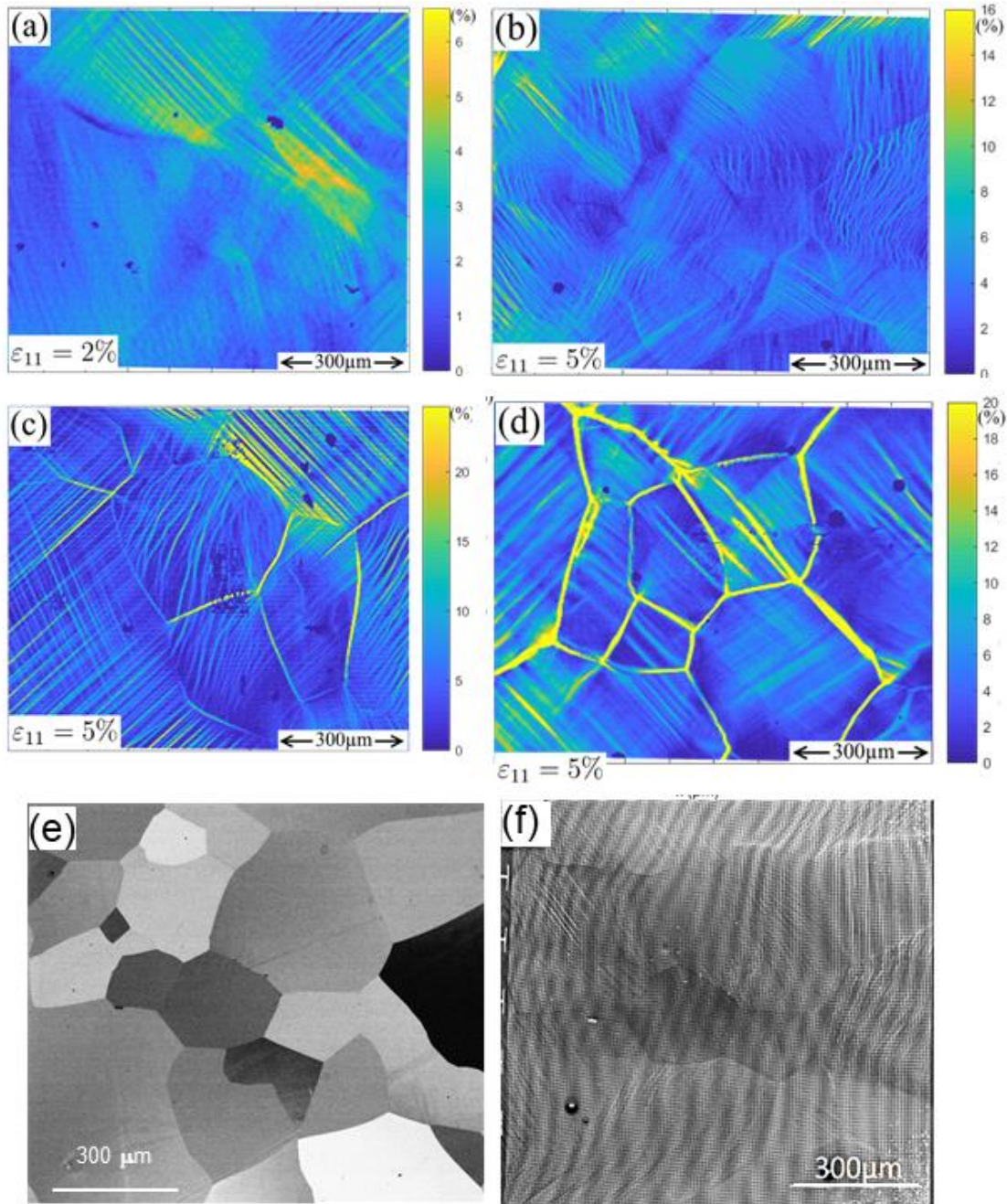


Figure 7: Typical computed strain maps and SEM micrographs of compression tests at ambient temperature and 2% axial strain (a), 0.4T<sub>m</sub>, 0.5T<sub>m</sub> and 0.6T<sub>m</sub> and 5% axial strain (b to d, respectively). Note, the strain maps (a to c) are not at the same color scale. e and f correspond respectively to SEM micrographs of the initial microstructure (Z-contrast, without marker grid) and the deformed state (SE contrast, with marker grid) of the sample compressed at 0.4T<sub>m</sub> (110°C).

Whilst the SEM micrographs have a spatial resolution of about 120 nm, the spatial resolution of the strain field mapping is limited by the micrometer-sized local strain gage. This limitation may be overcome by applying thin film metallic deposits onto the observation surfaces. Subsequent annealing at temperatures above 300°C leads to film cavitation, development of dendritic patterns and formation of metallic spheroid markers. Depending on film thickness, annealing temperature and time, the markers range from a few micrometers to a few tens of nanometers ([13], [26]). In our case however such refinement of spatial resolution is not mandatory, because the grain size is large (ca 300  $\mu\text{m}$ ).

The DIC-computed strain maps for samples deformed up to ca 5% at 110, 200 and 300°C clearly show temperature-related differences of localization patterns. At moderate and intermediate temperatures (110°C and 200°C, respectively) we can see some similarities and some differences. At first, it is worthy to note that in both cases slip lines are essentially sharp. At moderate temperature the spatial density of slip lines is high, but their strain intensity is low, and little localization of strain is detected at grain boundaries (Fig. 7a). At intermediate temperature (200°C) strain intensity of individual slip lines increases, whilst their spatial density decreases. Strong localization appears along several grain boundaries (Fig. 7b). At moderate temperature most of the grains present both wavy and straight slip morphology. At high temperature (300°C, Fig. 7c) slip lines present mostly straight, but diffuse character. They broaden considerably, but lose their sharpness. These morphological features may be related to recovery processes which are increasingly active with temperature. At room temperature crystal plasticity occurs by easy octahedral slip. At moderate temperatures (100 - 200°C) are active both octahedral easy slip, non-octahedral slip, and/or cross slip. Thermally activated non octahedral slip and cross-slip in FCC metals is largely reported in the literature ([27], [28], [29], [30], [31], ([32]) and is evidenced in the present work by the appearance of wavy slip lines, as shown in Figure 7. Recovery processes such as formation of dislocation walls and sub-grain boundaries involve dislocation climb and are therefore slow at moderate temperatures. As a result, dislocation densities increase. Gliding dislocations from different slip systems are mutually pinning which induces strain hardening (Fig. 6). This effect may be moderated if the width of the slip bands spreads, which in turns decreases the amount of crystallographic slip carried by individual slip planes. Conversely, at higher temperatures (300°C) dislocation climb processes are active, thus allowing for recovery and limiting strain hardening (Fig. 6). Therefore, crystal slip may be efficiently localized within few narrow slip bands. Very similar recent observations are reported for NaCl single crystals deformed at room and high temperature ([33]).

Most importantly, at high temperatures (300°C) all grain boundaries present very strong localization, related to grain boundary sliding (GBS). In this case, very large in-plane and out-of-plane components are observed on SEM micrographs and by AFM measurements (Fig. 8). Out-of-plane GBS induces the development of strong topography, and in some cases grain thrusting. In this case the surface marking pattern is partly lost due to grain overlapping. In other cases, the in-plane GBS component is so important that marking patterns are

extremely stretched and damaged. For these reasons, the DIC computation of strain along grain boundaries obtained at 300°C might be considered only as a lower bound. It is worth noting that GBS is usually invoked for superplastic behavior and is mostly associated with small grain sizes of the order of a few tens of  $\mu\text{m}$  or less ([7], [34], [35], [36], [37]). In the present study we clearly evidence and quantify by DIC the activity of GBS during in situ SEM hot-compression of nearly pure, massive and coarse-grained aluminum. Using similar techniques, a recent study identified GBS in columnar, coarse grained and high purity aluminum, subjected to in situ SEM traction ([11]). In spite of different experimental conditions, materials and microstructures, the consistency of the experimental observations suggests the ubiquity of GBS. A previous study based on DIC analysis of in situ SEM compression testing of synthetic rock salt have shown that GBS contribution to the overall strain increases with decreasing grain size ([13]). For coarse microstructures comparable to ours GBS contribution to the overall strain of rock salt was estimated to be of less than 10 % ([13], [14]). However, for rock salt deformed at room temperature GBS involves grain boundary decohesion and frictional sliding, leading to micro-damage and dilation ([14]), whilst in our case GBS is fully ductile.

At high temperature we also observed grain boundary migration (GBM), which is involved in dynamic recrystallization and high-temperature recovery mechanisms. The GBM driving forces in hot-deforming polycrystals relate to the different plastic strains accommodated across the grain boundary and the resulting difference in stored elastic strain energy. In our case (low strain) GB migration is not observed up to 200°C. It happens modestly at 300°, but starts to be pronounced at 400°C. Interestingly, the surface marking grid remains preserved during GBM, which indicates underlying diffusive mechanisms. DIC is inherently suited to low strain and modestly evolving microstructures. Conversely, marked GB migration is associated with strong evolution of the starting microstructure, which complicates the DIC analysis. When considering the cumulative strain with respect to the initial state as reference, GB migration results in artificially spread localization along the migrating portions of sliding grain boundaries, as shown in Figures 7d, 8c and 9. The step by step incremental kinematic analysis remains possible though, when referring to a previous loading step as reference.

GB migration may operate at small scales and strains, being coupled with limited relative grain displacement, which is known as shear coupled GB migration. All the experimental and numerical studies addressing this mechanism are based on TEM observations and atomistic scale simulations of particular grain boundaries. The involved grain boundary defects are called disconnections and are also operational at low temperature ([38], [39], [40], [41]). While being an important phenomenon involved in dynamic recrystallization and grain growth processes in polycrystalline materials, GB migration itself is beyond the scope of this study and we will not elaborate further on it.

Previous DIC based analysis of ductile deformation of synthetic rock salt ([13], [14]) have shown that GBS and CSP mechanisms are concomitant. However, for a coarse grained microstructure (ca 300  $\mu\text{m}$ ) CSP was

the dominant mechanisms, while GBS contributed with only a few percent to the overall strain. Both mechanisms were shown to accommodate each other. GBS was active along boundaries where plastic incompatibilities between neighboring grains occurred. Conversely, GBS resulted in strong localization at triple junctions, relating to activation of CSP in the grain facing the sliding interface, but also to diffuse micro-cracking.

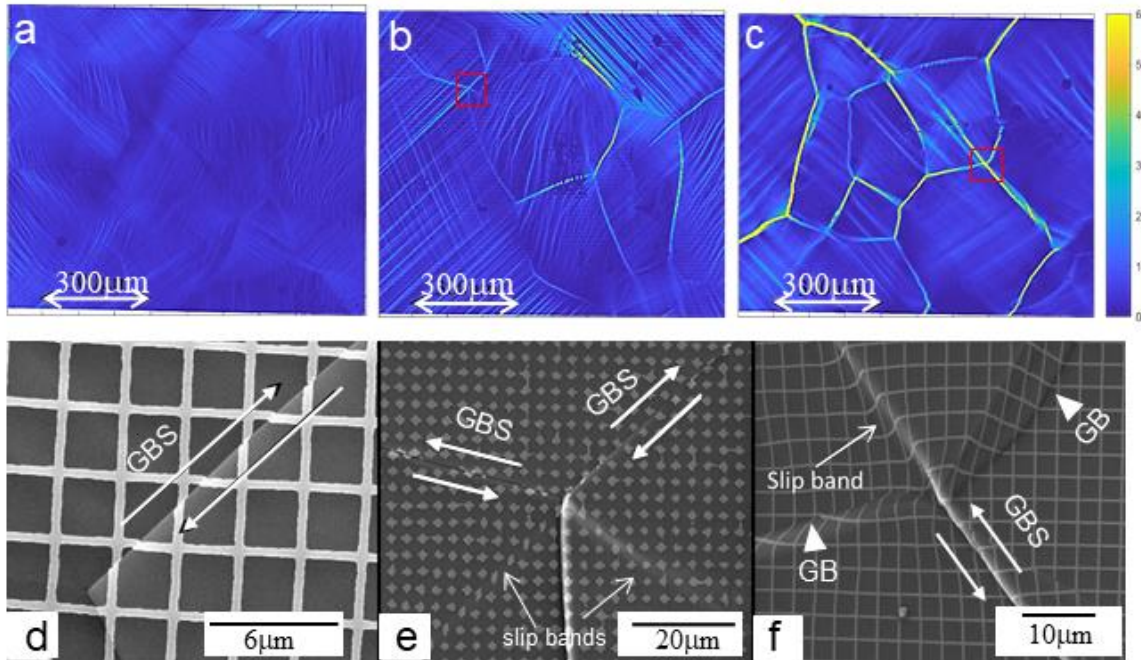


Figure 8: a, b and c: Same strain maps as in Figure 7 (for samples deformed at 0.4, 0.5 and 0.6  $T_m$  up to 5% axial strain), but shown with the same color scale. It is evidenced that increasing temperature results in lower spatial density of slip lines, but in higher intensity of slip (see text), which means higher localization. Grain boundary sliding is also strongly enhanced by temperature. d, e and f: SE mode micrographs of selected triple junctions, respectively from the same specimens as in a, b and c. At 0.4  $T_m$  little grain boundary sliding is evidenced. At higher temperature, this mechanism is accompanied by intense crystal slip activity within the third grain, which is facing the sliding grain boundary and acts as an incompatibility for GBS. The orientation of the third grain will strongly impact the GBS ability.

From a phenomenological point of view, GBS in hot-deformed fine grained materials is essentially the dominant deformation mechanism, while CSP, GB migration and/or diffusional mass transfer act as secondary local accommodation mechanisms at multiple grain junctions ([34] to [37]). Conversely, coarse grained materials are dominated by CSP and the phenomenon of GBS may be seen as an accommodation mechanism across interfaces where CSP transmission from a grain to another is limited due to crystallographic incompatibilities. Yet, the phenomenology of GBS may refer to different microphysical mechanisms active along GBs, including diffusional transfer, dislocation activity, or micro-damage and frictional sliding. The latter case was demonstrated in coarse grained rock salt by 2D and 3D full mechanical fields measurements, computed on the basis of DIC and

DVC (digital volume correlation, [14]). At room temperature the rock salt specimens presented substantial GBS activity involving diffuse micro-damage related to grain boundary decohesion and frictional sliding, as demonstrated by the DVC computed dilatant behavior. In fact, GBS was attributed to CSP incompatibilities across interfaces in relation with the large discrepancies between the critical resolved shear stresses of the different slip systems ([33]). In opposition, at temperatures where the different critical resolved shear stresses become comparable, the hot-deformed rock salt materials presented substantially lower GSB contribution ([14]). In the present study, the material is fully ductile, yet we do observe similar phenomena of interacting GBS and CSP, as shown in Figures 8 and 10.

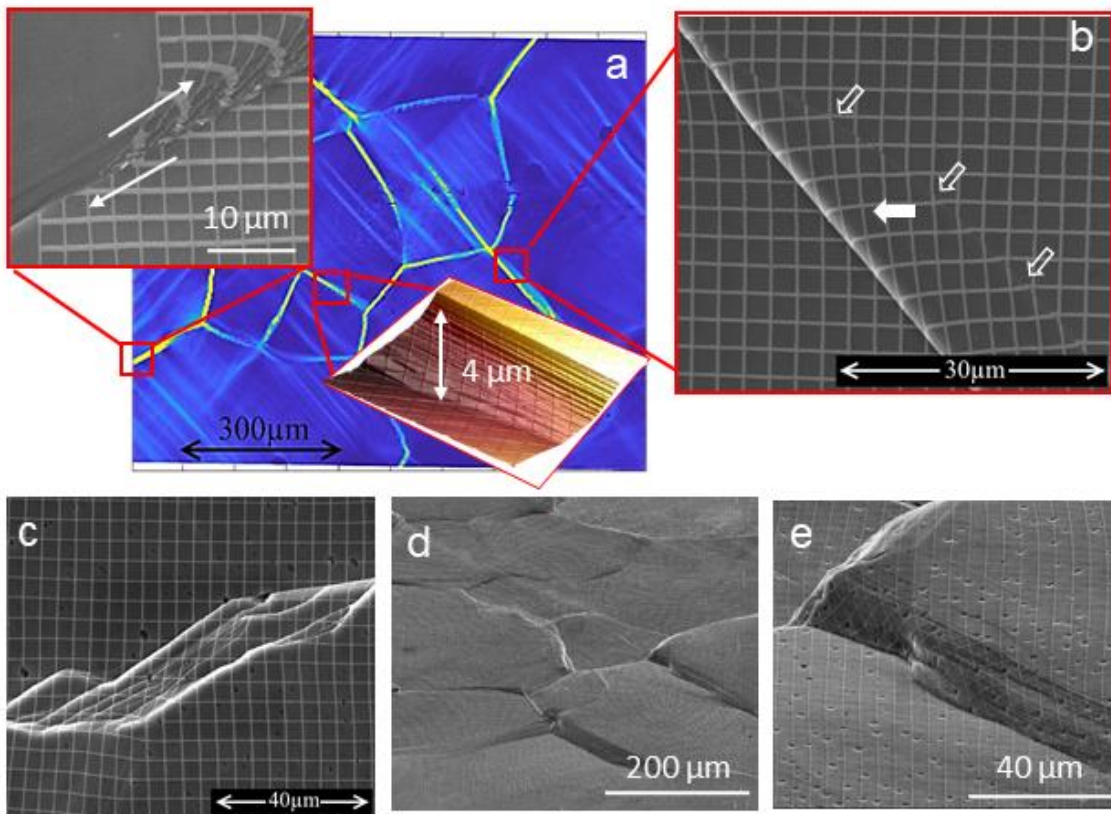


Figure 9: Intense GBS at 300°C (a and b) and 400°C (c, d, e) leads to development of marked topography (a, d and e) and grain boundary migration (b and c). Above 300°C the GBS is so active that the marking grid may be severely distorted/damaged (a). Continuous (b) or step-wise (c) grain boundary migration occurs, leading to substantial local microstructural modification of the interfaces. Very important out of plane grain sliding and grain overlapping, clearly evidenced by observing tilted samples (d, e), lead to damage and/or to loss of marker grid. All these phenomena may substantially complicate DIC computation (see text).

### 3.2. Strain localization evolution

DIC allows to show either the cumulative evolution of strain localization in reference to the initial state, or the incremental evolution by referring to each previous loading step. Figures 9a and 9b show the central ROI-1 with surface marking before and after deformation at 200°C. Some grains are labelled for the purpose of discussion. The Figures 10c to 10f show the cumulative development of strain localization at loading steps 2, 4, 7 and 10 corresponding respectively to c.a. 0,5%, 1.5 %, 3% and 5% macroscopic shortening. Interestingly, we can see in Figure 10c (step 2) that the early strain localization occurring right after yielding corresponds simultaneously to both crystal slip and GBS: the upward and downward solid arrows points respectively to a slip band and GBS. At this very early stage of deformation localization appears as straight slip bands in favorably oriented grains (like  $g_1$ ,  $g_4$ ,  $g_5$  or  $g_6$ ), which activate only single octahedral slip as evidenced by EBSD and geometrical analysis of slip traces (e.g. solid upward arrow pointing to (111) traces in c). At about 1.5 % axial strain (step 4, Fig. 10d), localization patterns clearly affect all of the grains, combining both CSP and GBS. At this stage, unfavorably oriented grains like  $g_2$ ,  $g_3$  and  $g_7$  activate non-octahedral cross-slip, as evidenced by the wavy slip bands denoted by horizontal arrows. Figures 10e and 10f (c.a. 3% and 5% shortening, respectively) show that increasing overall strain results in increasing density and intensity of slip bands in all grains. Double octahedral slip activates in favorably oriented grains, whilst the non-octahedral slip intensifies within unfavorably oriented ones. It is noteworthy that plastic compatibility between neighboring grains may be ensured simultaneously by both transmission of crystal slip across grain boundaries and by GBS, as indicated by the NE-SW solid arrows in Figure 10e. But, the interplay involves different weights for each mechanism. The ability of easy crystal slip transmission across grain boundaries (apparent continuity of straight slip bands) conditions the intensity of the GBS component. This one is low when the neighboring grains present strong plastic compatibility, as evidenced by apparent continuity of easy slip bands across the grain boundary (as for grains  $g_4$  and  $g_5$ , indicated by the NE-SW oriented hollow arrow in Fig. 10e). Conversely, the GBS component is high when the neighboring grains present stronger plastic incompatibility, as for grains  $g_2$  and  $g_6$  (indicated by the NW-SE oriented hollow arrow in Fig. 10e). These observations are qualitatively similar to previous ones in polycrystalline rock salt and suggest that the coexisting CSP and GBS mechanisms complement each other.

Intense slip bands originate from triple junctions facing sliding grain boundaries, as indicated by solid arrows in Fig. 10f. Most triple junctions are concerned with more than one sliding boundary. Therefore, they exhibit more than one originating slip band, each facing an adjacent sliding grain boundary. Conceptually, one or more cinematically required partner mechanisms must activate when GBS activates between two grains. In fact, an accommodation mechanism must activate at the triple junction facing the sliding grain boundary. GBS may be accommodated either by local diffusional mass transfer ([36], [37]) or by the formation of micro-cracks and/or

triple junction cavitation ([13], [43]). In these cases, the material might present respectively interfacial migration and dilatant behavior. Another option is the development of a localized CSP band starting from the concerned triple junction and propagating within the facing third grain. Such examples are shown in Figures 10c to 10f. A comparison of the evolution of intensity of the easy octahedral slip bands developing in grain g1 shows that the intensity of the slip band facing the grain boundary between grains g6 and g7 relates directly to the intensity of GBS along this interface. It is not clear whether a CSP band emerging at a triple junction is able to activate GBS along a facing grain boundary.

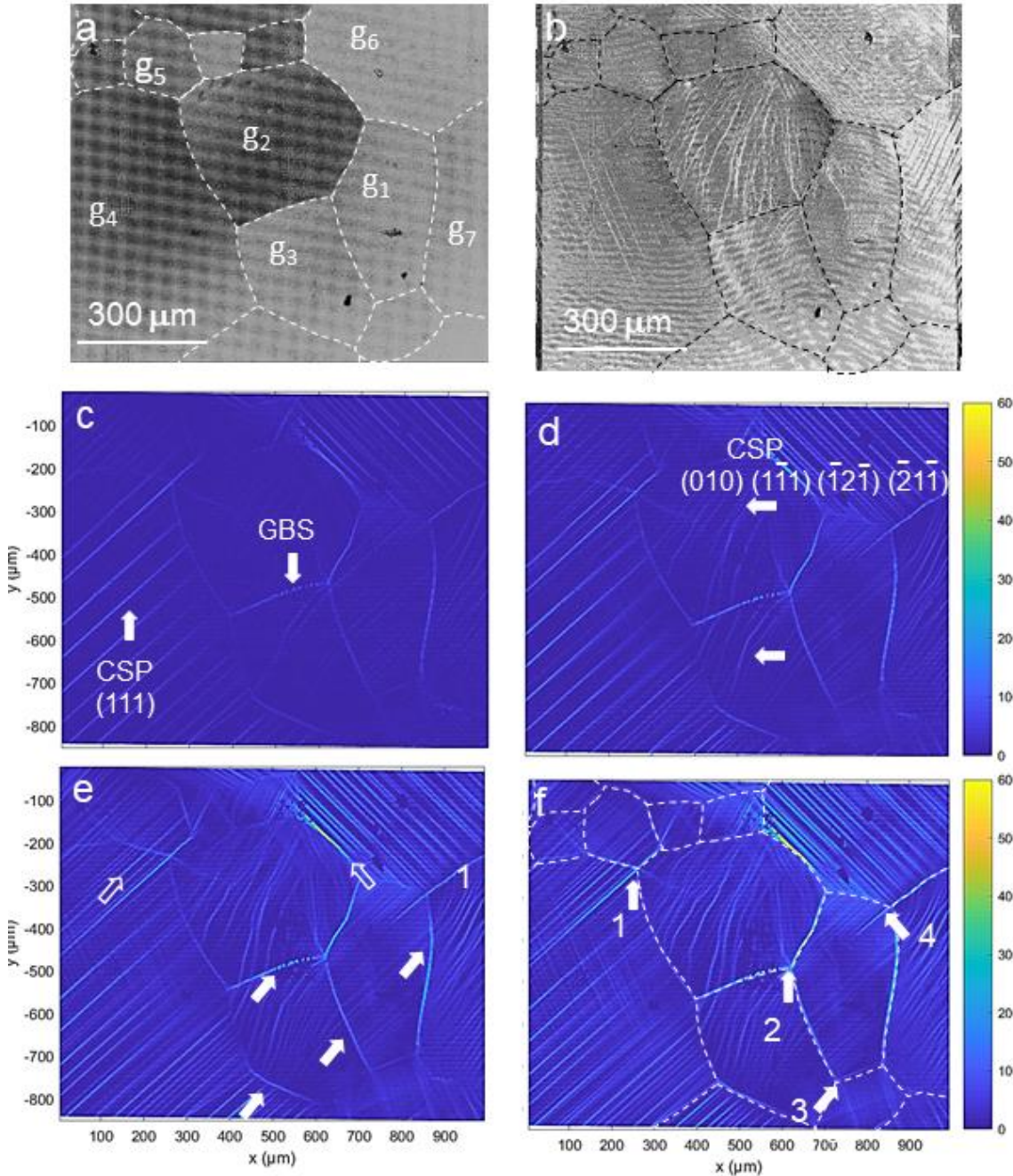


Figure 10. SEM micrographs of the microstructure of a ROI-I (a and b) and associated strain maps. For clarity, grain boundaries are represented on some images by dashed lines. a: The selected ROI-1 is observed in Z-contrast mode, showing the initial microstructure. Individual grains are labelled. b: The same microstructure is shown in SE mode after compression at 200°C (0.5 Tm) up to 5 % global shortening. Strongly enhanced image contrast evidences the physical slip lines. c, d, e and f: Equivalent strain maps corresponding to the same ROI-1 at deformation steps 1, 4, 7 and 10 (respectively c.a. 0.5, 1.5, 3 and 5 % axial strain), with respect to the initial reference image (cumulative strain fields). It is observed that both CSP and GBS activate right after yielding (upward and downward solid arrows points respectively to a slip bands and GBS in c). The activity of both mechanisms intensify with time. Easy octahedral slip is activated first (straight slip lines in c), followed by cross-slip as evidenced by the wavy slip lines (d to f). The compatibility of neighboring grains with respect to easy crystal slip transmission across the grain boundaries conditions the intensity of the GBS component. Grains  $g_4$  and  $g_5$  (indicated by the NE-SW oriented hollow arrow in Fig. 10e) involve little GBS, but strong continuity of easy slip band transmission across the interfaces. GBS component is high for grains  $g_2$  and  $g_6$  (indicated by the NW-SE oriented hollow arrow in Fig. 10e), which exhibit strong incompatibility with respect to easy slip.

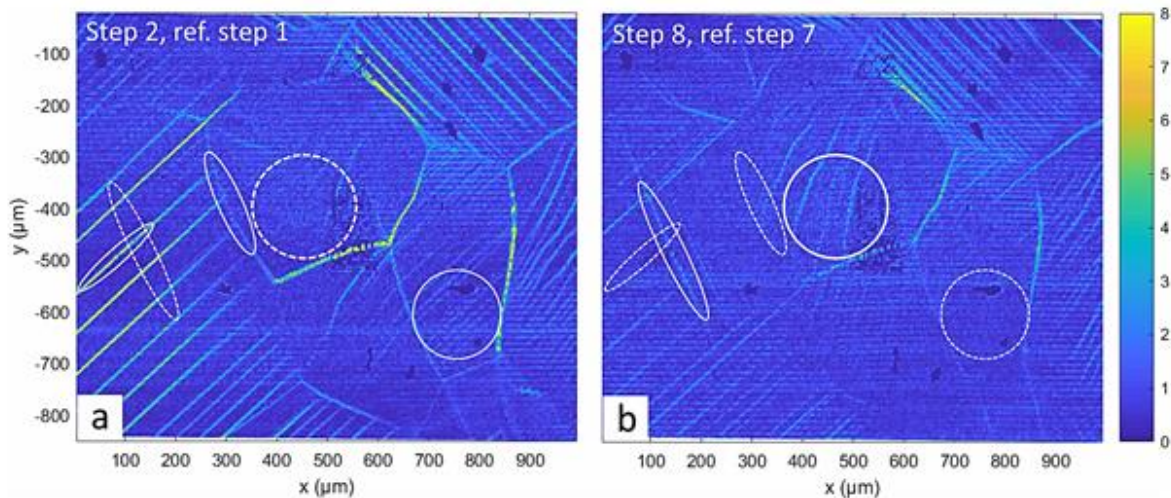


Figure 11: Strain maps for two steps of compression at 200 °C (a and b) with their previous step of deformation as reference. The white ellipses highlight the slip bands and the grain boundaries that slide, which appear and disappear on strain maps during the deformation. (a) Step at 0.5% of axial strain, increment of 0.4% from the previous (reference) step. (b) Step at 3% of axial strain, increment 0.44% from the previous step.

It is noteworthy that GBS activity is variable from a sliding interface to another. In addition, a variation of the GBS amplitude along a single interface is also observed, with maximum intensity in the central part of the grain boundary and lower intensities towards the ending triple junctions. Strain compatibility in polycrystals and gradient of GBS activity along sliding interfaces were theoretically addressed [40]. Experimental observation of such gradients were recently reported for pure aluminum with columnar microstructure [11].

The incremental evolution of strain localization obtained by DIC in reference to each previous loading step is shown in Figure 11. This approach allows to have a better representation of time resolved evolution of localization and hence of mechanisms activities and interactions. It is observed that the activity of crystal slip is discontinuous with time. The intensity of localization of slip bands is not monotonously increasing with loading.

For instance, some previously activated slip bands may have periods of inactivity and reactivate later on. Although less pronounced, a similar conclusion may be drawn for GBS too. Both mechanisms present history dependent activities. For example, in Figure 11 the solid and dashed line ellipses show respectively the emplacements of intermittent localization for both GBS and CSP, the dashed line ellipses denoting the lack of activity previously indicated by the solid line ellipses. The cumulative strain representation exhibited in Figure 10f shows several grains where i) the spatial distribution of slip lines is nearly homogeneous, ii) the intensity of individual slip lines is nearly homogeneous. Conversely, the step by step evolution of strain shown in Figure 11 demonstrates that both phenomena present sequential fluctuations along the loading history. It also appears that once activated, easy octahedral slip directly results in the formation of slip lines extending across the whole grain, whilst non-octahedral cross-slip generates slip lines which extend progressively all along the loading process.

### **3.3. Subsurface microstructure investigated by FIB and TEM**

The in situ SEM investigations give access to surface kinematic analysis, but the 3D microstructure in depth remains unknown. The observed slip traces and the crystallographic orientations of the individual grains obtained by EBSD allow to identify the active slip systems by simple geometric analysis, based on the determination of the resolved shear stresses and the corresponding most favorable Schmid factors. Conversely, geometrical analysis of GBS in terms of resolved shear stresses is difficult because the inclination of the GB plane in depth is unknown. Numerous grain boundary planes are inclined within the 3D microstructure, which is demonstrated by the observed out plane sliding components.

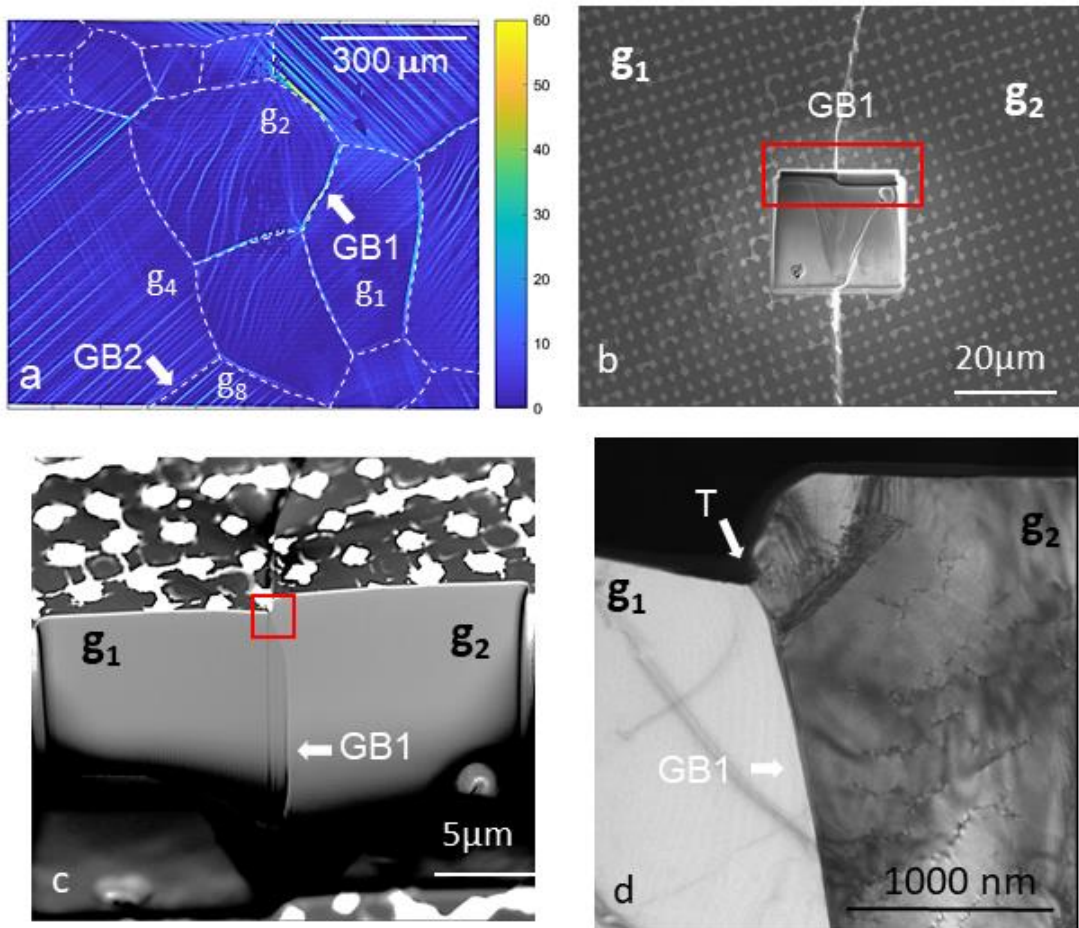


Figure 12: a: Final equivalent strain field of the sample shown in Fig. 10 and 11. The grain boundaries between grains  $g_1$  and  $g_2$  and between grains  $g_4$  and  $g_8$ , that we call GB1 and GB2 show respectively important and little GBS activity. b: The GB1 is observed in the dual beam SEM-FIB (the marker pattern is a grid of regularly spaced micrometer-sized spots). The excavation at the central part of the interface is operated by FIB milling. c: Imaging of the cross section of the grain boundary from aside (tilted specimen). Note that GB1 is nearly vertical at depth, except in the very vicinity of the surface, where it is moderately inclined to the left (see text for comments). Note also that parallel to GB1 there is a straight vertical trace within grain  $g_1$ , starting at the trace of GB1 on the sample surface, which is due to a milling artefact. d: TEM bright field micrograph from a thin slice taken by FIB-machining from the near surface region of the GB shown in c (red frame). Grain  $g_1$ , which is favorably oriented (Fig. 10 and 11) for easy octahedral slip, appears free of crystal defects in the vicinity of the grain boundary. Conversely,  $g_2$  is unfavorably oriented (see Fig. 10 and 11) and activates both octahedral and non-octahedral cross slip. It shows substantially high density of free dislocations, entangled dislocations and dislocation arrays. The surficial triple point representing the GB trace in the SEM observation plane is indicated. It is a source of free dislocations gliding in grain  $g_2$ . In depth,  $g_2$  is building a sub-grain boundary.

Sophisticated techniques such as DCT (diffraction contrast tomography) give access to the 3D crystallographic microstructure, which reliably match with the surficial EBSD data ([42]). These techniques need however access to synchrotron radiation. Furthermore, their spatial resolution is poorer with respect to SEM and TEM, which precludes the identification of structural crystallographic defects along grain boundaries that may be

involved in the GBS phenomenon. We therefore tried to capture some aspects of sliding interfaces using FIB (focused ion beam) machining and *post mortem* TEM investigations, in order to characterize GB's morphology at depth and dislocation microstructures in the vicinity of GB's, respectively.

We used focused ion beam (FIB Helios-660) to mill small volumes of about  $100 \mu\text{m}^3$  around specific GBs of interest, where GBS was identified and quantified (Figure 12a). The excavation allows to reveal the geometry of the GB at depth, and in particular its inclination. We observed that GBs presenting essentially in-plane sliding are nearly perpendicular to the observation plane as shown in Figures 12b and 12c. Secondly, we excavated cross section lamellae of  $\sim 20 \mu\text{m}$  long,  $\sim 10 \mu\text{m}$  large and  $\sim 2 \mu\text{m}$  thick across the chosen GBs. Platinum films were deposited onto the surficial top edges of the lamellae, in order to protect the trace of the GBs during ion milling. The machined lamellae were further thinned with a Gatan PIPS II and were observed with a Titan-Femis 300 kV TEM (CIMEX platform). In Figures 12 and 13 we show TEM micrographs of the grain boundary region between grains g1 and g2, from the sample deformed at  $200^\circ\text{C}$  shown in Figures 10 and 11. These Figures show that grains g1 and g2 present substantial differences in terms of strain field intensity and morphology, which translate differences in crystal plasticity mechanisms. The slip lines of grain g1 indicate mostly easy octahedral slip with little out of plane components, whilst g2 exhibits octahedral and non-octahedral cross-slip with considerably large out of plane components. The implications are that the slip systems active in g1 do not interfere, whilst those active in g2 would indubitably interact and result in more complex and entangled dislocation microstructures. This is precisely what we observed in TEM, as shown in Figures 12 and 13. Figure 12d shows a TEM micrograph from the upper most part of the grain boundary GB1 (corresponding to the red frame in Fig. 12c). We can see at the triple point T between g1, g2 and the free surface the bulging of grain g2 with respect to grain g1, which may be simply due to thermal grooving of the grain boundary, or it may represent a small amount of out of plane GBS. The most striking observation is the lack of inherited dislocation microstructures in g1, whilst g2 presents both numerous free dislocations and several complex dislocation arrays. Figure 13 is focusing in the area of the triple point T, which represents the actual trace of GB1 at the surface of the massive sample observed by SEM. Figure 13a show several dislocations emitted from T, gliding towards a sub-surface dislocation array. Figure 13b shows that the latter represents a sub-grain boundary (SGB) composed of two sets of parallel dislocations. The intimate mechanism involved in the GBS itself still remains unclear. However, the striking difference of dislocation microstructures in g1 and g2 indicate that the plastic incompatibility between the two grains might in turns be the reason for GBS activation. In addition, we observed that GB1 is slightly migrating at the expense of g2. The migration is demonstrated by GB1's curvature in the vicinity of the sample surface, whilst it remains straight and vertical at depth (Fig. 12c). It is reported in literature that GB thermal grooving significantly affects grain growth in the vicinity of free surfaces. The triple junctions (T) of the GB grooves may partially or completely pin moving GBs ([44], [45]), hence inducing the characteristic

sub-surface curvatures of the migrating GB as shown in Figure 12c. GB1 migration may be seen as the result of the different dislocation densities between g1 and g2. The latter exhibits much higher dislocation density and hence the largest strain energy. The fact we observe simultaneously GBS and GB migration may indicate contribution of disconnections to the GBS phenomenon ([39] to [41]).

We further observed by TEM similar bi-crystalline lamellae, excavated from GBs of undeformed starting aluminum, or from GBs of the previously observed sample exhibiting very little GBS. We show in Figure 14 the TEM micrographs corresponding to an excavated lamella from GB2 (between g4 and g8, Figure 12a) and from a starting undeformed GB. Figure 14b shows very similar dislocation microstructures in both g4 and g8. Both grains present sub-grain boundaries and fewer free-dislocations. These observations and the local strain fields exhibited in Figures 10 and 11 indicate that grains g4 and g8 are plastically compatible, which might be the reason why GB2 shows very little GBS. Conversely, Figure 14c shows that the GBs in the starting undeformed material do not present GB grooving, nor dislocation arrays and very few free dislocations.

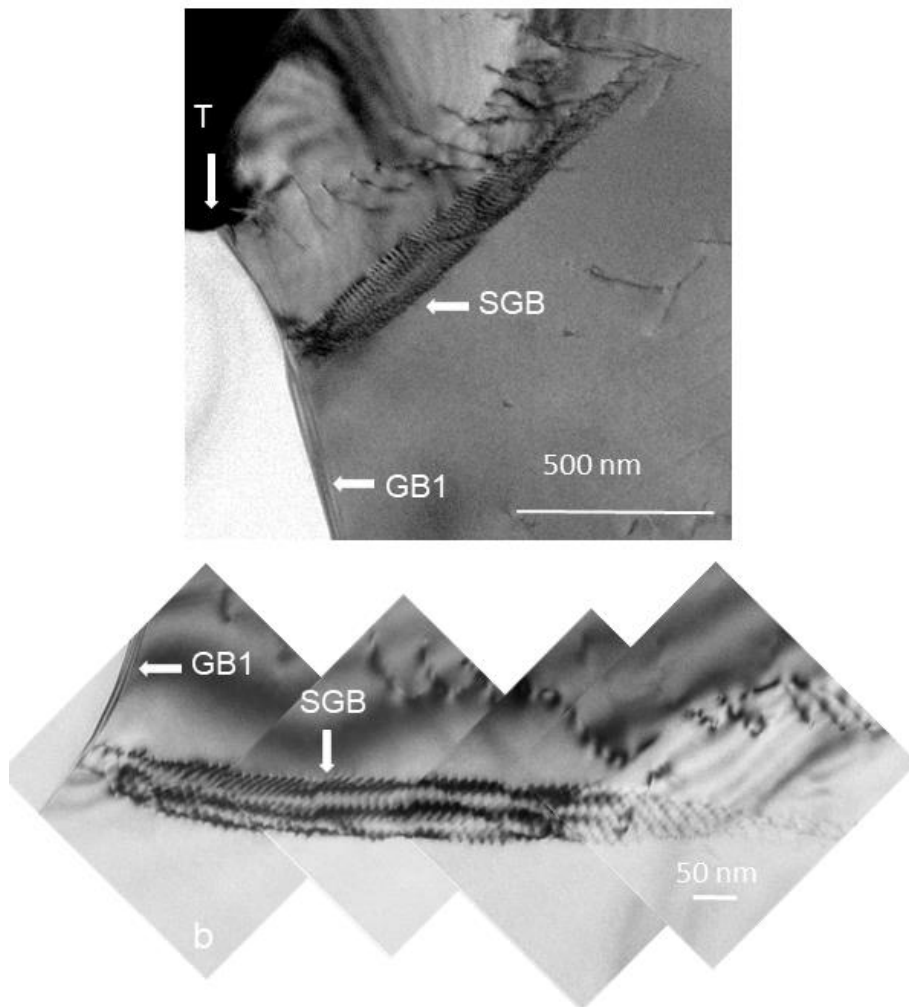


Figure 13: a and d: Higher magnification TEM micrographs from the same slice as in Figure 12d. a: The sub-grain boundary (SGB) in g2 is initiating at the grain boundary between grains g1 and g2 (GB1, see Fig. 12). The triple junction T is the source of a series of free dislocations, piling up at the SGB. b: The SGB is shown in more details, evidencing two sets of constitutive dislocation families.

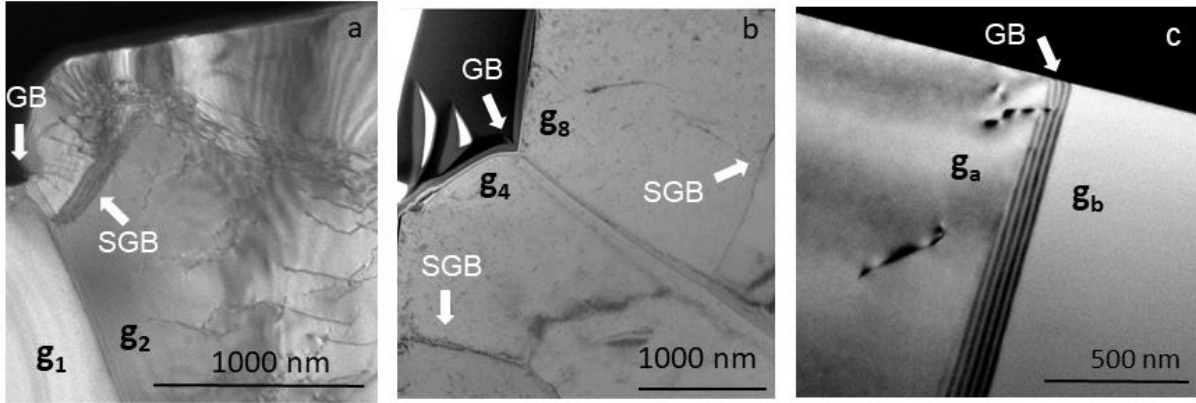


Figure 14: TEM micrographs from selected GBs in a sample deformed at 200°C (a,b) and in an undeformed sample (c). a: Image across the grain boundary GB1, between g1 and g2 (Fig. 11 to 13). The micrograph shows numerous free dislocations in g2 and a sub-grain boundary(SGB) ending at GB1. But, g1 is dislocation free (see also Fig. 12 and 13). b: Image across GB2, between g4 and g8 (Fig. 11 to 13). Both grains show equivalent dislocation microstructures, with sub-grain boundaries. Both GB1 and GB2 exhibit surface grooving. c: Image across a GB in undeformed sample of the same material as in a and b. There is no GB grooving and very few free dislocations. Note, that the grain boundary (GB) is not exactly oriented edge-on, and is showing fringes indicative of the slice thickness.

Our observations do not determine unambiguously the operational mechanisms of the GBS phenomenon. Simultaneously GBS and GB migration may indicate contribution of disconnections ([39] to [41]). Conversely, GBS may also involve diffusional mass transfer along GBs. Dislocation activity at GBs may also contribute. It is admitted now that specific dislocation mechanisms occur at grain boundaries and movements of dislocations inside the grain boundaries have been observed. Apart from movement of single dislocations, we should also consider more complex assemblies, such as pileups at the grain boundary, which have been pointed out by DDD (discrete dislocation dynamics) studies coupled to Laue micro-diffraction experiments ([46]). Such dislocation structures initiating at a sliding grain boundary may be at the origin of sub-grain boundaries such as the one we report in Figure 13. Our micrographs drive at exploring more boundaries, which can be an incentive to envisage additional dislocation microstructures at grain boundaries.

### 3.4. Conclusions

The original setup presented in this work allowed to perform multi-scale full mechanical field measurements in-situ SEM, coupling hot compression tests and DIC analysis. Detailed analysis of the localization patterns allowed to discriminate the deformation mechanisms activated during viscoplastic flow of coarse grained

aluminum specimens at room conditions and temperatures of up to 400°C, and at constant displacement loading of about 0.1  $\mu\text{ms}^{-1}$  corresponding to a strain rate of about  $10^{-5} \text{ s}^{-1}$ . Deformation was largely dominated by crystal plasticity, starting mostly with octahedral easy slip at room temperature, then progressively activating non-octahedral cross slip with increasing temperature. Localization intensity of slip increases with temperature, whilst its spatial distribution decreases, which suggests strong thermal healing and recovery effects. Concomitantly, minor component of GBS activates above 100°C and progressively increases with temperature. Above 300°C GBS becomes very pronounced and induces strong out-of-plane grain sliding resulting in strong topography and grain thrusting. Similarly, grain migration phenomena become noticeable. Both phenomena limit the possibilities of kinematic analysis by DIC. Most importantly, GBS and CSP simultaneously activate right after yielding, at axial strains of less than half a percent. GBS intensity seems to correlate with crystal slip incompatibility between neighboring grains, which observations indicate that for coarse grained aluminum GBS is a secondary but necessary mechanisms allowing to accommodate local plastic incompatibilities. These observations are further supported by TEM investigations of dislocation microstructures along sliding grain boundaries. Otherwise, severely localized CSP starts from triple junctions and extends within grains facing sliding boundaries. The net result is a continuous interplay between the two mechanisms, allowing the achievement of macroscopically homogeneous viscoplastic flow.

**Funding:** This work has been supported by the Fondation EDF, sponsoring the Chaire "Energies durables" under the supervision of Franck Carré.

On behalf of all authors, the corresponding author states that there is no conflict of interest.

### **Acknowledgements**

We thank Vincent de Greef, Erik Guimbretière, Hakim Gharbi and Jean Christophe Eytard for their precious technical support. We also warmly thank Romain Quey (Lab. George Friedel, Ecole des Mines de Saint Etienne) for kindly providing the aluminum alloy and Eva Héripré (MSSMAT, Ecole Centrale Supélec) for access and help with the FIB.

### **Conflict of Interest Statement**

On behalf of all authors, the corresponding author states that there is no conflict of interest.

## References

- [1] M Kawasaki. and T.G. Langdon: *J. Mater. Sci.*, 2007, vol. 42, pp. 1782-96.
- [2] F. Ashby: *Acta Metall.*, 1972, vol. 20, pp. 887-97.
- [3] F. Ashby: *Adv. Appl. Mech.*, 1982, vol. 23, pp. 117-77.
- [4] H. J. Frost and M. F. Ashby: *Deformation Mechanism. Maps: The Plasticity and Creep of Metals and Ceramics*, Pergamon Press, Oxford, New York, 1982, 166 pp.
- [5] J. Weertman: *J. Appl. Phys.*, 1957, vol. 28, pp. 1185-89.
- [6] J. Weertman: *J. Appl. Phys.*, 1957, vol. 28, pp. 362.
- [7] H. Lüthy, R.A. White, and O.D. Sherby: *Mat. Sci. Eng.*, 1979, vol. 39, pp. 211-16.
- [8] B. Fazan, O.D. Sherby, and J.E. Dorn: *J. Met.*, 1954, vol. 6, pp. 919-22.
- [9] T.R. Bieler, P. Eisenlohr, H.J. Phukan, and M.A. Crimp: *Curr. Opin. Solid State Mater. Sci.*, 2014, vol 18, pp. 212-26.
- [10] T.R. Bieler, R. Alizadeh, M. Peña-Ortega, and J. Llorca: *Int. J. Plast.*, 2019, vol. 118, pp. 269-90.
- [11] M.A. Linne, A. Venkataraman, M.D. Sangid, and S. Daly: *Exp. Mech.*, 2019, vol. 59, pp. 643–58.
- [12] R. Alizadeh, M. Peña-Ortega, T.R. Bieler, and Llorca, J.: *Scr. Mater.*, 2020, vol. 178, pp. 408-12.
- [13] M. Bourcier, M. Bornert, A. Dimanov, E. Heripre, and J.L. Raphanel: *J. Geophys. Res.: Solid Earth*, 2013, vol. 118, pp. 511–26.
- [14] A. Gaye, M. Bourcier, M. Bornert, E. Héripré, A. Dimanov, J. Raphanel, and K. Sab: *Am. Rock Mech. Assoc., ARMA, 2014, 48th US Rock Mechanics / Geomechanics Symposium, Minneapolis (USA)*.
- [15] N. Combe, F. Momprou, and M. Legros: *Phys. Rev. Mater.*, 2019, vol. 3, pp. 060601.
- [16] M.A. Sutton, N. Li, D.C. Joy, A.P. Reynolds, and X. Li, X.: *Exp. Mech.*, 2007, vol. 47, pp. 775–87.
- [17] J. Dautriat, M. Bornert, N. Gland, A. Dimanov, and J.L. Raphanel: *Tectonophysics*, 2011, vol. 503, pp. 100-16
- [18] E. Héripré, M. Dexet, J. Crépin, L. Gélébart, A. Roos, M. Bornert, and D. Caldemaison: *Int. J. Plast.*, 2009, vol. 23, pp. 1512-39.
- [19] A. Goyal, V. Doquet, and A. Pouya,: *Metall. Mater. Trans. A*, 2020, vol. 51, pp. 1109-22.
- [20] R. Quey, P. Dawson, and J.H. Driver: *IOP Conf. Ser.: Mater. Sci. Eng.*, 2015, vol. 89, 012011.
- [21] P. Doumalin, M. Bornert, and D. Caldemaison: *Proc. Int. Conf. on Advanced Technology in Experimental Mechanics, JSME*, 1999, vol. 1, pp. 81-86.
- [22] P. Doumalin, P. and M. Bornert: in: P. Jacquot, J.M. Fournier (Eds.), *Proc. Interferometry in Speckle Light: Theory and Applications*, Springer-Verlag, EPFL Lausanne, 2000, pp. 67-74.
- [23] A. Lens, A., Maurice, C. and Driver, J.H.: (2005), *Mater. Sci. Eng. A*, 2005, vol. 403, pp.144-53.

- [24] R. Quey, D. Piot, J.H. and Driver: *Acta Mater.*, 2010, vol. 58, pp. 1629-42.
- [25] A. Mecif, B. Bacroix, and P. Franciosi: *Acta Mater.*, 1997, vol. 45, pp. 371-81.
- [26] A. El Sabbagh : *Thèse de Doctorat en Mécanique des Matériaux de l'Ecole Polytechnique, Palaiseau*, 2018
- [27] B. Bacroix, and J.J. Jonas: *Texture, Stress, Microstruct.*, 1987, vol. 8, 957619.
- [28] A. Couret and D. Caillard: *Acta Metall.*, 1988, vol. 36, pp. 2515-24.
- [29] D. Caillard and J.L. Martin: *J. Phys. (Paris)*, 1989, vol. 50, pp.2455-73.
- [30] A. Albou, A. Borbely, C. Maurice, and J.H. Driver: *Phil. Mag.*, 2011, vol. 91, pp. 3981-4000.
- [31] D. Caillard and J.-L. Martin: *Int. J. Mater. Res.*, 2009, vol. 100, pp. 1403-10.
- [32] R. Le Hazif and J.-P. Poirier: *Acta Metall.*, 1975, vol. 23, pp. 865-71.
- [33] D. Picard, A. Dimanov, and J.L. Raphanel: *Mat. Sci. Eng. A.*, 2018, vol. 732, pp. 284-97.
- [34] C.N. Ahlquist and R.A. Menezes: *Mater. Sci. Eng.*, 1971, vol. 7, pp. 223-24.
- [35] T.G. Langdon: *Phil. Mag.*, 1971, vol. 21, pp. 689-700.
- [36] M.F. Ashby and R.A. Verall: *Acta Metall.*, 1973, vol. 21, pp. 149-63.
- [37] R. Raj and M.F. Ashby: *Metall. Trans.*, 1971, vol. 2, pp. 1113–27.
- [38] A. Rajabzadeh, F. Momprou, S. Lartigue-Korinek, N. Combe, M. Legros, M., and D.A. Molodov: *Acta Mater.*, 2014, vol. 77, pp. 223-35.
- [39] N. Combe, F. Momprou, M. Legros: *Phys. Rev. B: Condens. Matter and Mater. Phys.*, 2016, vol. 93, pp. 024109.
- [40] N. Combe, F. Momprou, and M. Legros: *Phys. Rev. Mater.*, 2019, vol. 3, pp. 060601.
- [41] M. Larranaga, F. Momprou, M. Legros, and N. Combe: *Phys. Rev. Mater.*, 2020, vol. 4, pp.123606.
- [42] N. Vigano, A. Tanguy, S. Hallais, A. Dimanov, M. Bornert, K.J. Batenburg, and W. Ludwig: *Sci. Rep.*, 2016, vol. 6, pp.1-9.
- [43] A. Dimanov, G. Dresen, E. Rybacki, and R. Wirth: *J. Struct. Geol.*, 2007, vol. 29, pp. 1049-69.
- [44] Y. Palizdar, D. San Martin, M. Ward, R.C. Cochrane, R. Brydson, and A.J. Scott: *Mater. Charact.*, 2013, vol. 84, pp. 28-33.
- [45] M. Verma and R. Mukherjee: *J. Appl. Phys.*, 2021, vol. 130, pp. 025305.
- [46] G. Daveau : *Thèse Ecole Centrale, Paris*, 2012, <https://tel.archives-ouvertes.fr/tel-00740650>.